

Controlled-source electromagnetic modelling using high order finite-difference time-domain method on a nonuniform grid

Pengliang Yang¹ and Rune Mittet²

¹School of Mathematics, Harbin Institute of Technology, Harbin, China, 150001

E-mail: ypl.2100@gmail.com

²Norwegian University of Science and Technology (NTNU), Norway

E-mail: mittet.rune@gmail.com

December 2, 2022

Abstract

Simulation of 3D low-frequency electromagnetic fields propagating in the Earth is computationally expensive. We present a fictitious wave domain high-order finite-difference time-domain (FDTD) modelling method on nonuniform grids to compute frequency-domain 3D controlled-source electromagnetic (CSEM) data. The method overcomes the inconsistency issue widely present in the conventional 2nd order staggered grid finite difference scheme over nonuniform grid, achieving high accuracy with arbitrarily high order scheme. The finite-difference coefficients adaptive to the node spacings, can be accurately computed by inverting a Vandermonde matrix system using efficient algorithm. A generic stability condition applicable to nonuniform grids is established, revealing the dependence of the time step and these finite-difference coefficients. A recursion scheme using fixed point iterations is designed to determine the stretching factor to generate the optimal nonuniform grid. The grid stretching in our method reduces the number of grid points required in the discretization, making it more efficient than the standard high-order FDTD with a densely sampled uniform grid. Instead of stretching in both vertical and horizontal directions, better accuracy of our method is observed when the grid is stretched along the depth without horizontal stretching. The efficiency and accuracy of our method are demonstrated by numerical examples.

1 Introduction

Marine controlled source electromagnetics (CSEM) provides valuable information about subsurface resistivities and therefore potentially about pore fluids or rocks. It is very useful to decipher subsurface properties to assist energy exploration, in particular when combined with seismic data. The CSEM technology relies on low-frequency electromagnetic field propagation to probe the subsurface. The low-frequency electromagnetic (EM) field propagation does not lend itself to an intuitive understanding in the same manner as seismic field propagation does due to the diffusive nature of the EM field in conductive media. Thus, three-dimensional modeling becomes an important tool for the interpretation of CSEM data. Imaging of marine CSEM data is today mainly done by inversion of the observed electric and/or magnetic fields.

The kernel of CSEM inversion is the numerical simulation of 3D electromagnetic field propagation, which is computationally expensive. Reducing the simulation time without compromising the accuracy is important. It can shorten the turnaround time for an imaging project while reducing the investments in computer hardware. The implementation of nonuniform grid schemes is a well known strategy to reduce simulation time. To retain good accuracy we propose a high-order finite-difference approach.

There are many studies on diffusive electromagnetic modelling using different methods. Examples are the frequency-domain finite-difference method (Newman and Alumbaugh, 1995; Smith, 1996a; Mulder, 2006; Streich, 2009), the frequency-domain finite-element method (Li and Key, 2007; da Silva et al., 2012; Key, 2016; Rochlitz et al., 2019), and the time-domain finite-difference method (Oristaglio and Hohmann, 1984; Wang and Hohmann, 1993; Taflove and Hagness, 2005). A key fact in all numerical modelling methods is that the computational cost and the memory requirement are connected and cannot be splitted. A method can be very efficient if more computer memory is available. The efficiency and accuracy of the modelling can be dramatically hampered when the available computer resources are restricted.

Due to the diffusive nature of low-frequency CSEM fields, most of the 3D CSEM modelling schemes resort to the frequency-domain solution of the Maxwell equation to avoid the high computational cost dictated by the

restrictive stability condition for the direct solution in the time domain. Time-domain methods are attractive options because they require less amount of memory than frequency-domain modelling within a model of the same size. Another advantage with time-domain solutions is that multiple frequencies can be extracted from the same simulation. Both the frequency-domain finite-difference method and the frequency-domain finite-element method formulate Maxwell equation as a linear equation system, which may be solved using direct (Streich, 2009) or iterative (Smith, 1996b; Mulder, 2006; Puzyrev et al., 2013) solvers. A nice feature with a direct solver is that multiple right-hand sides are fast to calculate after the system matrix has been factorized or inverted. However, there are significant implementation challenges with this approach when realistic size marine CSEM surveys are simulated. The memory requirements are large even if the equation system is sparse.

The finite-difference time-domain (FDTD) modelling based on the staggered grid proposed by Yee (1966) has for several decades been a main workhorse for many EM applications. The implementation of the numerical core is straight forward and the computational efficiency is good for wave phenomena. The computational efficiency for diffusive phenomena is rather poor in the time domain. The system of partial differential equations can be considered stiff in this case (Mittet, 2010) and a very small time step is required to retain stability. The computational efficiency can be improved significantly due to a correspondence principle for wave and diffusion fields (Lee et al., 1989; de Hoop, 1996; Mittet, 2010). Maaø (2007) proposed a mixed wave and diffusion-domain FDTD method to perform numerically efficient CSEM modelling. This method allowed for large time steps compared to a purely diffusion-domain solution. Mittet (2010) proposed a high-order FDTD scheme by utilizing the fictitious wave to diffusion-domain transformation. The simulation is performed in the wave domain where the propagation velocity is proportional to the square root of resistivity.

The Yee grid (staggered grid) FDTD scheme is often the method of choice due to a good agreement with physics. It gives divergence free magnetic fields and electric currents (Smith, 1996a). This standard scheme proposed by Yee (1966) is based on the second-order approximation of the first derivatives assuming an equispaced mesh. On the uniform grid, moving from second-order FDTD to high-order FDTD is straight forward (Mittet, 2010), and gives improved modelling accuracy due to the reduction of spatial dispersion errors. To improve the modelling efficiency, the use of nonuniform grid is widespread (Newman and Alumbaugh, 1995; Mulder, 2006), however it results in inconsistencies for the grid staggering. As illustrated in Figure 1, this inconsistency leads to only first-order local truncation error, even though the global accuracy may be up to second order (Monk and Sili, 1994). The problem is persistent and has remained unresolved for high-order schemes.

We propose an efficient 3D CSEM simulation method with high accuracy using *high-order FDTD on a staggered, nonuniform grid*, following the fictitious wave domain approach (Mittet, 2010). To resolve the inconsistency issue in conventional 2nd order staggered grid approach, our key recognition is that the order of local truncation error can be arbitrarily high also on a nonuniform grid if the finite-difference operator coefficients are adapted properly to the variable grid spacing. The derivative operator coefficients are calculated by inverting a Vandermonde matrix system.

To gain good modeling efficiency, we transform the diffusive Maxwell equation into the fictitious wave domain. The efficiency of the method is restricted by stability condition: the stepsize in time is proportional to the inverse of the propagation velocity of the field, affected by the node spacing. The gridding of the same physical domain leads to different number of gridpoints, affecting the size of the linear system to be solved. The use of nonuniform grid helps to reduce the number of gridpoint, thus reducing the computational cost. Unfortunately, the stability condition for high order FDTD over non-uniform grid is non-trivial. An important contribution of this paper is to establish a new stability condition valid for arbitrarily high order FDTD scheme on nonuniform grid. The stability condition shows the strong dependence between time step and the finite difference coefficients computed by inverting the Vandermonde matrix. This is not known in EM geophysics community, as far as we know.

To generate the optimal grid using a power law, we design a recursion scheme using fixed point iterations to find the optimal stretching factor. We prove the recursion scheme is guaranteed to converge. The optimal factor found by the recursive scheme allows accurate matching of the computational domain using given number of mesh points. The high accuracy and efficiency of this high-order FDTD method on a nonuniform grid will be exemplified by a number of numerical tests using reference solutions.

2 Theory

We utilize the correspondence principle for electromagnetic wave and diffusion fields (Lee et al., 1989; de Hoop, 1996; Mittet, 2010) to calculate the CSEM response efficiently. The key to a high-order local truncation error on a nonuniform grid relies on the solutions to a Vandermonde system giving derivative operator coefficients that adapts to local grid properties. The stability condition is then established for FDTD modelling on the nonuniform grid.

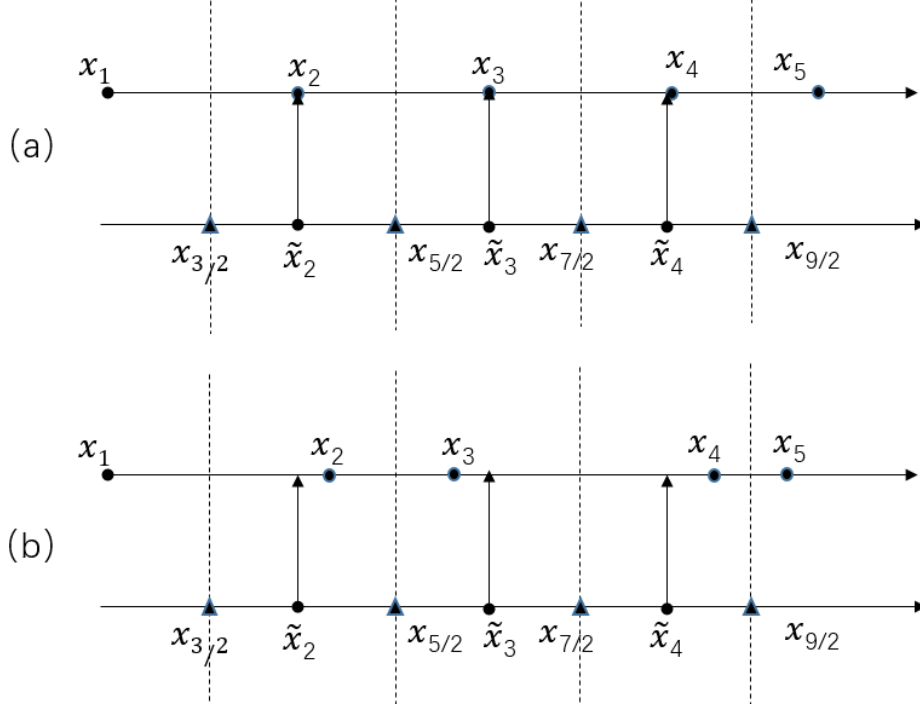


Figure 1: The 2nd order staggered-grid finite-difference scheme on (a) uniform grid and (b) nonuniform grid. The grid points on staggered grid are obtained by taking the midpoints from nonuniform grid to ensure the 2nd order accuracy. This accuracy is not guaranteed on nonuniform grid since the midpoints is inconsistent. For example, $x_{3/2} = (x_1 + x_2)/2$, $x_{5/2} = (x_2 + x_3)/2$, but $\tilde{x}_2 = (x_{3/2} + x_{5/2})/2 \neq x_2$ due to uniform grid spacing. This inconsistency leads to first-order local truncation error using staggered-grid finite-difference scheme on the nonuniform grid.

The Maxwell equations in a quasi-static regime (i.e., with negligible effect of displacement currents) are written in the time domain as

$$\begin{aligned}\nabla \times \mathbf{E} + \mu \partial_t \mathbf{H} &= -\mathbf{M}, \\ -\nabla \times \mathbf{H} + \sigma \mathbf{E} &= -\mathbf{J},\end{aligned}\tag{1}$$

or in the frequency domain as

$$\begin{aligned}\nabla \times \mathbf{E} - i\omega \mu \mathbf{H} &= -\mathbf{M}, \\ -\nabla \times \mathbf{H} + \sigma \mathbf{E} &= -\mathbf{J},\end{aligned}\tag{2}$$

where $\mathbf{E} = (E_x, E_y, E_z)^T$ and $\mathbf{H} = (H_x, H_y, H_z)^T$ are electric and magnetic fields. The magnetic permeability is μ . The conductivity is a symmetric 3×3 tensor: $\sigma_{ij} = \sigma_{ji}$, $i, j \in \{x, y, z\}$. An isotropic medium means that only the diagonal elements of the conductivity tensor are non-zeros and the same in all directions: $\sigma_{xx} = \sigma_{yy} = \sigma_{zz}$; $\sigma_{ij} = 0, i \neq j$. The vertical transverse isotropic (VTI) medium implemented here still has only diagonal elements, but the vertical and the horizontal conductivities may differ, i.e., $\sigma_h := \sigma_{xx} = \sigma_{yy}$, $\sigma_v = \sigma_{zz}$. We use the following Fourier transform convention, $\partial_t \leftrightarrow -i\omega$.

To speed up the FDTD modelling, we transform the above system from the diffusion to the wave domain, following Mittet (2010). The idea is to define a fictitious dielectric permittivity in equation 2 as $\sigma = 2\omega_0 \varepsilon$, yielding

$$\begin{aligned}\nabla \times \mathbf{E} - i\omega \mu \mathbf{H} &= -\mathbf{M}, \\ -\nabla \times \mathbf{H} + 2\omega_0 \varepsilon \mathbf{E} &= -\mathbf{J},\end{aligned}\tag{3}$$

which gives the following relation after multiplying the second equation with $\sqrt{-i\omega/2\omega_0}$

$$\begin{aligned}\nabla \times \mathbf{E} + \underbrace{\sqrt{-i2\omega\omega_0}}_{-i\omega'} \mu \underbrace{\sqrt{\frac{-i\omega}{2\omega_0}}}_{\mathbf{H}'} \mathbf{H} &= -\mathbf{M}, \\ -\nabla \times \underbrace{\sqrt{\frac{-i\omega}{2\omega_0}}}_{\mathbf{H}'} \mathbf{H} + \underbrace{\sqrt{-i2\omega\omega_0}}_{-i\omega'} \varepsilon \mathbf{E} &= -\underbrace{\sqrt{\frac{-i\omega}{2\omega_0}}}_{\mathbf{J}'} \mathbf{J},\end{aligned}\quad (4)$$

which translates into the wave and simulation domain as the time dependent system

$$\begin{aligned}\nabla \times \mathbf{E}' + \mu \partial_t \mathbf{H}' &= -\mathbf{M}', \\ -\nabla \times \mathbf{H}' + \varepsilon \partial_t \mathbf{E}' &= -\mathbf{J}'.\end{aligned}\quad (5)$$

We have introduced a prime to identify the fields in the wave domain.

From the electromagnetic fields in the wave domain, the frequency-domain fields can be computed on the fly during modelling using the fictitious wave transformation, exemplified by the electric field here,

$$\mathbf{E}'(\mathbf{x}, \omega') = \int_0^{T_{\max}} \mathbf{E}'(\mathbf{x}, t) e^{i\omega' t} dt, \quad (6)$$

where T_{\max} is the final time until the field $E'(\mathbf{x}, \omega')$ reaches its steady state and where

$$\omega' = (1 + i)\sqrt{\omega\omega_0}. \quad (7)$$

In order to have results valid for the frequency domain we need to calculate the Green's functions. We need the following relation,

$$\begin{aligned}\mathbf{E}' &= \mathbf{E}, \\ \mathbf{H}' &= \sqrt{\frac{-i\omega}{2\omega_0}} \mathbf{H}, \\ \mathbf{M}' &= \mathbf{M}, \\ \mathbf{J}' &= \sqrt{\frac{-i\omega}{2\omega_0}} \mathbf{J}.\end{aligned}\quad (8)$$

The Green's functions are then obtained by normalizing the transformed electric and magnetic fields with the source current,

$$\begin{aligned}G_{kj}^{E|J}(\mathbf{x}, \omega | \mathbf{x}_s) &= \frac{E_k(\mathbf{x}, \omega | \mathbf{x}_s)}{J_j(\omega)} = \sqrt{\frac{-i\omega}{2\omega_0}} \frac{E'_k(\mathbf{x}, \omega | \mathbf{x}_s)}{J'_j(\omega)}, \\ G_{kj}^{H|J}(\mathbf{x}, \omega | \mathbf{x}_s) &= \frac{H_k(\mathbf{x}, \omega | \mathbf{x}_s)}{J_j(\omega)} = \frac{H'_k(\mathbf{x}, \omega | \mathbf{x}_s)}{J'_j(\omega)},\end{aligned}\quad (9)$$

where $G_{kj}^{E|J}(\mathbf{x}, \omega | \mathbf{x}_s)$ and $G_{kj}^{H|J}(\mathbf{x}, \omega | \mathbf{x}_s)$ stand for the electrical and magnetic Green's function for angular frequency ω at spatial location \mathbf{x} with the source located at \mathbf{x}_s .

Equation 4 is a pure wave-domain equation and the time integration can easily be discretized using the leap-frog method. We let the time be $t_n = n\Delta t$ with n the integer time variable and Δt the time step. We also introduce $N = n + \frac{1}{2}$ such that,

$$\begin{aligned}\mathbf{H}'^N &= \mathbf{H}'^{N-1} + \Delta t \mu^{-1} (-\nabla \times \mathbf{E}'^n - \mathbf{M}'^n), \\ \mathbf{E}'^{n+1} &= \mathbf{E}'^n + \Delta t \varepsilon^{-1} (\nabla \times \mathbf{H}'^N - \mathbf{J}'^N).\end{aligned}\quad (10)$$

The time integration of these equations is second-order accurate. It is shown in Mittet (2010) that the calculation of the desired fields in the "real world" diffusive domain is independent of the frequency content of the source term used for calculating the fictitious fields. We exploit this fact and achieve good accuracy for the time integration by transmitting a low-frequency signal in the fictitious wave domain. Here we are concerned with the spatial part of the simulation scheme so we turn to this topic next.

We use a similar notation for the space variables as for the time variables where we write $x_i = x_{i-1} + \Delta x_i$ where Δx_i is the node separation between node x_{i-1} and node x_i . Likewise, we assume a forward staggered

grid such that $x_I = x_{I-1} + \Delta x_I$ where Δx_I is the node separation between node x_{I-1} and node x_I . For a uniform staggered grid we have a constant node separation such that $\Delta x_I = \Delta x_i = \Delta x$ and $I = i + \frac{1}{2}$. The y and z directions can be described in the same way with lower case and upper case integer arguments.

Calculation of the partial derivative of the field $f(x)$ can, in the continuous case, be formulated as an integral operator by

$$\partial_x f(x) = \int_{-\infty}^{\infty} dx' f(x+x') \{-\partial_{x'} \delta(x')\} = \int_{-\infty}^{\infty} dx' f(x+x') \alpha(x'). \quad (11)$$

The discrete formulation, with $f(x_i) := f(i)$, is,

$$\partial_x f(x_i) \approx D_x f(i) = \sum_{l=-L}^L f(i+l) \alpha_l(i), \quad (12)$$

where $\alpha_l(i)$ is a band-limited approximation to the operator $\alpha(x')$ in equation 11. The half length of the operator is L . The argument i is used to explicitly show that this operator will vary with location for a nonuniform grid. For the staggered grid, we can then define discretized forward, D_x^+ , and backward, D_x^- , derivative operators as,

$$\begin{aligned} D_x^+ f(i) &= \partial_x f(I) = \sum_{l=1}^L f(i+l) \alpha_l(i) - f(i-l+1) \alpha_{-l}(i), \\ D_x^- f(I) &= \partial_x f(i) = \sum_{l=1}^L f(I+l-1) \alpha_l(I) - f(I-l) \alpha_{-l}(I), \end{aligned} \quad (13)$$

which is the form we need for nonuniform grids and which is investigated here. The f' implies spatial derivative in equation 13.

The operator simplifies for uniform grids where the operator becomes independent of spatial location such that $\alpha_l(i) = \alpha_{-l}(i) = \alpha_l$

$$\begin{aligned} D_x^+ f(i) &= \partial_x f(I) = \sum_{l=1}^L (f(i+l) - f(i-l+1)) \alpha_l, \\ D_x^- f(I) &= \partial_x f(i) = \sum_{l=1}^L (f(I+l-1) - f(I-l)) \alpha_l. \end{aligned} \quad (14)$$

If we use $L = 1$ we have that $\alpha_1 = 1/\Delta x$ and equation 14 formulates the well known second-order accurate partial derivative operations,

$$\begin{aligned} D_x^+ f(i) &= \partial_x f(I) = (f(i+1) - f(i))/\Delta x, \\ D_x^- f(I) &= \partial_x f(i) = (f(I) - f(I-1))/\Delta x. \end{aligned} \quad (15)$$

Let us assume a non-magnetic subsurface so that μ has the same value as in the vacuum, $\mathbf{M} = 0$, while ϵ is a diagonal tensor $\epsilon = \text{diag}(\epsilon_{ii}), i = x, y, z$. The staggering is as in Mittet (2010),

$$\begin{aligned} H'_x{}^N(i, J, K), \quad H'_y{}^N(I, j, K), \quad H'_z{}^N(I, J, k), \\ E'_x{}^n(I, j, k), \quad E'_y{}^n(i, J, k), \quad E'_z{}^n(i, j, K), \\ J'_x{}^n(I, j, k), \quad J'_y{}^n(i, J, k), \quad J'_z{}^n(i, j, K), \\ \epsilon_{xx}(I, j, k), \quad \epsilon_{yy}(i, J, k), \quad \epsilon_{zz}(i, j, K), \end{aligned} \quad (16)$$

and the scheme implemented is,

$$\begin{aligned}
H'_x{}^N &= H'_x{}^{N-1} - \frac{\Delta t}{\mu} (D_y^+ E'_z{}^n - D_z^+ E'_y{}^n), \\
H'_y{}^N &= H'_y{}^{N-1} - \frac{\Delta t}{\mu} (D_z^+ E'_x{}^n - D_x^+ E'_z{}^n), \\
H'_z{}^N &= H'_z{}^{N-1} - \frac{\Delta t}{\mu} (D_x^+ E'_y{}^n - D_y^+ E'_x{}^n), \\
E'_x{}^{n+1} &= E'_x{}^n + \frac{\Delta t}{\epsilon_{xx}} (D_y^- H'_z{}^N - D_z^- H'_y{}^N - J'_x{}^N), \\
E'_y{}^{n+1} &= E'_y{}^n + \frac{\Delta t}{\epsilon_{yy}} (D_z^- H'_x{}^N - D_x^- H'_z{}^N - J'_y{}^N), \\
E'_z{}^{n+1} &= E'_z{}^n + \frac{\Delta t}{\epsilon_{zz}} (D_x^- H'_y{}^N - D_y^- H'_x{}^N - J'_z{}^N).
\end{aligned} \tag{17}$$

The conventional second-order staggered grid FDTD scheme discretizes the spatial derivatives as follows (Newman and Alumbaugh, 1995; Mulder, 2006):

$$\begin{aligned}
D_y^- H'_z &= \frac{H'_z(I, J, k) - H'_z(I, J - 1, k)}{\Delta y_J}, & D_z^- H'_y &= \frac{H'_y(I, j, K) - H'_y(I, j, K - 1)}{\Delta z_K}, \\
D_z^- H'_x &= \frac{H'_x(i, J, K) - H'_x(i, J, K - 1)}{\Delta z_K}, & D_x^- H'_z &= \frac{H'_z(I, J, k) - H'_z(I - 1, J, k)}{\Delta x_I}, \\
D_x^- H'_y &= \frac{H'_y(I, j, K) - H'_y(I - 1, j, K)}{\Delta x_I}, & D_y^- H'_x &= \frac{H'_x(i, J, K) - H'_x(i, J - 1, K)}{\Delta y_J}, \\
D_y^+ E'_z &= \frac{E'_z(i, j + 1, K) - E'_z(i, j, K)}{\Delta y_j}, & D_z^+ E'_y &= \frac{E'_y(i, J, k + 1) - E'_y(i, J, k)}{\Delta z_k}, \\
D_z^+ E'_x &= \frac{E'_x(I, j, k + 1) - E'_x(I, j, k)}{\Delta z_k}, & D_x^+ E'_z &= \frac{E'_z(i + 1, j, K) - E'_z(i, j, K)}{\Delta x_i}, \\
D_x^+ E'_y &= \frac{E'_y(i + 1, J, k) - E'_y(i, J, k)}{\Delta x_i}, & D_y^+ E'_x &= \frac{E'_x(I, j + 1, k) - E'_x(I, j, k)}{\Delta y_j},
\end{aligned} \tag{18}$$

where Δx_i , Δy_j and Δz_k are distances between nodes on the reference grid, while Δx_I , Δy_J and Δz_K are the distance between the grid points (I, j, k) and $(I - 1, j, k)$, the distance between the grid points (i, J, k) and $(i, J - 1, k)$, and the distance between the grid points (i, j, K) and $(i, j, K - 1)$. This scheme is second-order accurate on a uniform grid with $\Delta x_i = \Delta x_I$ and likewise for the other spatial directions. The scheme is consistent with using equation 14 with $L = 1$ to approximate the derivatives.

A standard discretization method for nonuniform grids is to use the same formulation as above, but where the node distance may vary along the same spatial direction. It is well known that there are accuracy issues with this implementation. To achieve second-order accuracy using equation 14 is not possible. The midpoints between nodes do not align after going from the reference grid to the staggered grid and back again. Since $\Delta x_i \neq \Delta x_I$, we have a situation where the cell center does not match on a nonuniform grid, as is illustrated in Figure 1b. Consequently, the local truncation error of the resulting scheme can only reach first order. Reduced accuracy will also be a problem if we implement a high-order FDTD scheme ($L > 1$) on a nonuniform grid, using derivative-operator coefficients designed for a regular grid. This is unfortunate since the nonuniform grid is potentially attractive for efficient modelling due to significant reduction of the number of grid point. However, good accuracy can be restored if equation 13 is used instead of equation 14. The problem that remains is to calculate the operator coefficients for equation 13.

2.1 Vandermonde matrix

The major difference between FDTD implementations on a uniform grid and on a nonuniform grid lies in the design of the spatial-derivative operator coefficients. The position of each field component on the nonuniform staggered grid has been illustrated in Figure 2, which is similar to the staggered FDTD on a uniform grid.

In order to compute the electromagnetic field as well as its derivatives with arbitrary grid spacing, we have to do a polynomial interpolation using a number of knots x_0, x_1, \dots, x_n . According to the Taylor expansion,

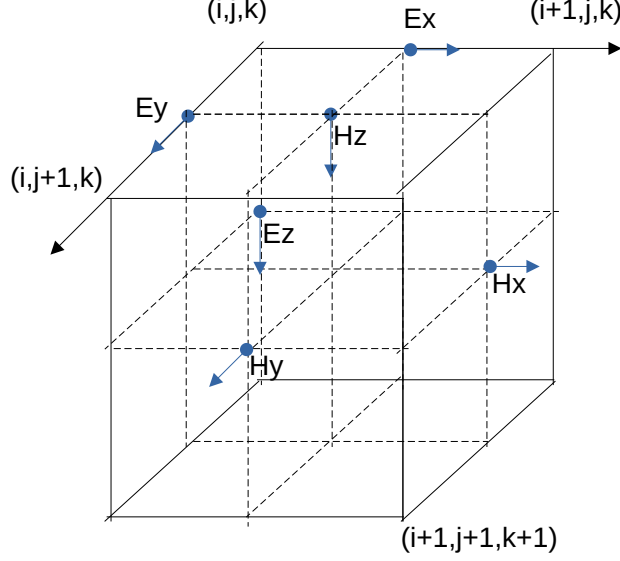


Figure 2: Electrical and magnetic fields on staggered grid (Yee, 1966).

we have

$$f(x_i) = f(x) + f'(x)(x_i - x) + \frac{1}{2}f''(x)(x_i - x)^2 + \dots + \frac{1}{n!}f^{(n)}(x)(x_i - x)^n + \dots \quad (19)$$

$$i = 0, 1, \dots, n.$$

By defining $a_i(x) := f^{(i)}(x)/i!$, we end up with a polynomial of the Newton form,

$$f(x_i) = a_0(x) + a_1(x)(x_i - x) + a_2(x)(x_i - x)^2 + \dots + a_n(x)(x_i - x)^n + \dots \quad (20)$$

$$i = 0, 1, \dots, n.$$

Let us consider $n + 1$ distinct nodes x_0, x_1, \dots, x_n and drop the terms $O((x_i - x)^{n+1})$. This builds a matrix system

$$\underbrace{\begin{pmatrix} f(x_0) \\ f(x_1) \\ \vdots \\ f(x_n) \end{pmatrix}}_{\mathbf{f}} = \underbrace{\begin{pmatrix} 1 & x_0 - x & (x_0 - x)^2 & \dots & (x_0 - x)^n \\ 1 & x_1 - x & (x_1 - x)^2 & \dots & (x_1 - x)^n \\ \dots & \dots & \dots & \dots & \dots \\ 1 & x_n - x & (x_n - x)^2 & \dots & (x_n - x)^n \end{pmatrix}}_{\mathbf{V}^T(x_0 - x, \dots, x_n - x)} \underbrace{\begin{pmatrix} a_0(x) \\ a_1(x) \\ \vdots \\ a_n(x) \end{pmatrix}}_{\mathbf{a}}, \quad (21)$$

where $\mathbf{V}^T(x_0 - x, \dots, x_n - x)$ is the transpose of a Vandermonde matrix determined by $x_0 - x, \dots, x_n - x$. The above expression implies that the function $f(x)$ and its derivatives up to the n -th order at arbitrary location x can be found by inverting the Vandermonde matrix: $(f(x), f'(x), \dots, f^{(n)}(x)/n!)^T = \mathbf{a} = [\mathbf{V}^T]^{-1}\mathbf{f}$.

It is well known that the Vandermonde matrix is highly ill-conditioned and direct matrix inversion by Gaussian elimination should be avoided due to numerical instabilities when the matrix size becomes large. Fortunately, there exists an efficient algorithm based on the method of Björck and Pereyra (1970) to invert the Vandermonde matrix. In fact, the algorithm circumvents the curse of severe ill-conditioning of the Vandermonde matrix to arrive at arbitrarily high accuracy for the inversion (Demmel and Koev, 2005). Compared with Gauss-elimination of complexity $O(n^3)$, the Vandermonde matrix inversion algorithm reduces the computational complexity to $O(n^2)$. Because the elements of the Vandermonde matrix are fully determined by the interpolation nodes, there is no need to explicitly construct the matrix and store it before inversion. The detailed implementation of this fast algorithm is available in Golub (1996, Algorithm 4.6.1).

Let the i -th row, j -th column of the inverse matrix $[\mathbf{V}^T]^{-1}$ be w_{ij} , i.e., $([\mathbf{V}^T]^{-1})_{ij} = w_{ij}$, $i, j = 0, \dots, n$. It

also follows that

$$\underbrace{\begin{pmatrix} a_0(x) \\ a_1(x) \\ \vdots \\ a_n(x) \end{pmatrix}}_{\mathbf{a}} := \underbrace{\begin{pmatrix} w_{00} & w_{01} & \cdots & w_{0n} \\ w_{10} & w_{11} & \cdots & w_{1n} \\ \vdots & & & \\ w_{n0} & w_{n1} & \cdots & w_{nn} \end{pmatrix}}_{[\mathbf{V}^T]^{-1}} \underbrace{\begin{pmatrix} f(x_0) \\ f(x_1) \\ \vdots \\ f(x_n) \end{pmatrix}}_{\mathbf{f}}. \quad (22)$$

The i -th row gives the explicit expression to find the i -th derivative

$$\frac{1}{i!} f^{(i)}(x) = a_i(x) = \sum_{j=0}^n w_{ij} f(x_j) = \langle w_i, \mathbf{f} \rangle, \quad i = 0, \dots, n. \quad (23)$$

The first row of the matrix $[\mathbf{V}^T]^{-1}$ (i.e., w_{0j} , $j = 0, \dots, n$) is $f(x)$ which in analogy with equation 11 can be written in discrete form as

$$f(x) = \int_{-\infty}^{\infty} dx' f(x+x') \{\delta(x')\} = \int_{-\infty}^{\infty} dx' f(x+x') \beta(x'). \quad (24)$$

The discrete formulation is,

$$f(x_i) = \sum_{l=-L}^L f(i+l) \beta_l(i), \quad (25)$$

where $\beta_l(i)$ are the coefficients for an interpolation operator adapted to a nonuniform grid and identical to the w_{0j} coefficients. The second row of the matrix $[\mathbf{V}^T]^{-1}$ (i.e., w_{1j} , $j = 0, \dots, n$) is $\partial_x f(x)$ and the continuous and discrete representations are given in equations 11 and 12. The $\alpha_l(i)$ coefficients are for a derivative operator adapted to a nonuniform grid and identical to the w_{1j} coefficients. To be explicit, consider the staggered finite-difference approximation of the first derivatives in x direction using $2L$ non-equidistant nodes. The finite-difference coefficients $\alpha_l(x_i)$ and $\alpha_l(x_I)$, $l = -L+1, \dots, L$ are the 2nd row of the inverse of the matrices $\mathbf{V}^T(x_{i+L}-x_I, \dots, x_{i-L+1}-x_I)$ and $\mathbf{V}^T(x_{I+L}-x_i, \dots, x_{I-L+1}-x_i)$. Using the $2L$ nodes, we achieve accuracy up to $2L$ -th order in space.

In general we find that the operator coefficients (interpolation weights) for $f^{(i)}(x)$ are $i!w_{ij}$. Given the points x_0, \dots, x_n and x , the Vandermonde matrix is determined and the operator coefficients can be calculated. For the simulation we only need the derivative-operator coefficients. It is noteworthy to mention that the Vandermonde matrix must be non-singular to be inverted. For the derivative-operator coefficients we have that the Vandermonde matrix is non-singular by construction of the staggered grids. A finite-difference scheme on a staggered grid implies that the node x_I , whose derivative is computed, will stay in the middle between the selected nodes x_i , which ensures that the resulting Vandermonde matrix is invertible.

The interpolation operators are useful for recording fields at arbitrary locations and for the distribution of source contributions (Mittet, 2017). Just as for the derivative-operator coefficients, the interpolation coefficients can be pre-calculated and then reused every time step. For the interpolation operator we may find that some of the coordinates x_i matches the interpolation points x , the inversion of Vandermonde matrix is then not necessary. This might happen when the source or receiver positions coincide with a finite-difference node. In this case, the interpolation weights w_{0i} to evaluate $f(x)$ should be exactly 1 at x_i and 0 elsewhere. In order to do 2D/3D simulation on nonuniform grid, multidimensional interpolant is simply constructed by tensor products of many 1D interpolants.

The above procedure is significant as it allows us to use arbitrarily high-order finite-difference scheme to accurately compute the electromagnetic fields and their derivatives, typically with arbitrary grid spacing in the rectilinear grid. This opens the door for CSEM modelling using high-order FDTD on a nonuniform grid in a consistent framework. The computed finite-difference coefficients may also be used to do high-order frequency-domain modelling on a nonuniform grid, while the resulting sparse banded matrix has to be solved accurately if sufficient computational resources are available.

2.2 Stability condition

Let us write down the FDTD scheme in equation 10 without source terms as follows:

$$\begin{cases} \mathbf{E}'^{n+1} = \mathbf{E}'^n + \Delta t \epsilon^{-1} \nabla \times \mathbf{H}'^N \\ \mathbf{H}'^{N+1} = \mathbf{H}'^N - \Delta t \mu^{-1} \nabla \times \mathbf{E}'^{n+1} \end{cases}, \quad (26)$$

leading to

$$\begin{bmatrix} \mathbf{E}'^{n+1} \\ \mathbf{H}'^{N+1} \end{bmatrix} = \underbrace{\begin{bmatrix} \mathbf{I} & \Delta t \epsilon^{-1} \nabla \times \\ -\Delta t \mu^{-1} \nabla \times & \mathbf{I} - \Delta t^2 \epsilon^{-1} \mu^{-1} \nabla \times \nabla \times \end{bmatrix}}_{\mathbf{A}} \begin{bmatrix} \mathbf{E}'^n \\ \mathbf{H}'^N \end{bmatrix}. \quad (27)$$

The numerical stability requires the eigenvalues of the amplification matrix \mathbf{A} to be less than or equal to 1. Assume the eigenvalue decomposition for the amplification matrix is $\mathbf{A} = \bar{\mathbf{V}} \mathbf{\Lambda} \bar{\mathbf{V}}^T$, where $\bar{\mathbf{V}} = (\mathbf{V}_E, \mathbf{V}_H)^T$ is an unitary matrix such that $\bar{\mathbf{V}}^T \bar{\mathbf{V}} = \mathbf{I}$. Then we have $\mathbf{A} \mathbf{V} = \mathbf{V} \mathbf{\Lambda}$, yielding

$$\begin{bmatrix} \mathbf{I} & \Delta t \epsilon^{-1} \nabla \times \\ -\Delta t \mu^{-1} \nabla \times & \mathbf{I} - \Delta t^2 \epsilon^{-1} \mu^{-1} \nabla \times \nabla \times \end{bmatrix} \begin{bmatrix} \mathbf{V}_E \\ \mathbf{V}_H \end{bmatrix} = \begin{bmatrix} \mathbf{V}_E \\ \mathbf{V}_H \end{bmatrix} \mathbf{\Lambda}. \quad (28)$$

That is,

$$\begin{cases} \Delta t \epsilon^{-1} \mu^{-1} \nabla \times \mathbf{V}_H = \mathbf{V}_E (\mathbf{\Lambda} - \mathbf{I}) \\ -\Delta t \mu^{-1} \nabla \times \mathbf{V}_E - \Delta t^2 \epsilon^{-1} \mu^{-1} \nabla \times \nabla \times \mathbf{V}_H = \mathbf{V}_H (\mathbf{\Lambda} - \mathbf{I}). \end{cases} \quad (29)$$

Multiplying the second sub equation $\mathbf{\Lambda} - \mathbf{I}$ from the right and inserting the first sub equation gives

$$-\Delta t^2 \mu^{-1} \epsilon^{-1} \nabla \times \nabla \times \mathbf{V}_H \mathbf{\Lambda} = \mathbf{V}_H (\mathbf{\Lambda} - \mathbf{I})^2. \quad (30)$$

Denote $\mathbf{V}_{H,j}$ the j th column of \mathbf{V}_H and λ_j the j th eigenvalue in $\mathbf{\Lambda}$. The above equation reads

$$\mu^{-1} \epsilon^{-1} \nabla \times \nabla \times \mathbf{V}_{H,j} = -\frac{(\lambda_j - 1)^2}{\Delta t^2 \lambda_j} \mathbf{V}_{H,j}, \quad (31)$$

which shows that $-\frac{(\lambda_j - 1)^2}{\Delta t^2 \lambda_j}$ is the eigenvalue of the matrix $(\mu \epsilon)^{-1} \nabla \times \nabla \times$ associated with the eigenvector $\mathbf{V}_{H,j}$. This leads to

$$(\lambda_j^2 + (-2 + \Delta t^2 c^2 \nabla \times \nabla \times) \lambda_j + 1) \mathbf{V}_{H,j} = (\lambda_j^2 - (2 + \Delta t^2 c^2 \Delta) \lambda_j + 1) \mathbf{V}_{H,j} = 0, \quad (32)$$

where we denote $c := 1/\sqrt{\mu \epsilon}$ and have applied $\nabla \times \nabla \times \mathbf{F} = \nabla \nabla \cdot \mathbf{F} - \nabla \cdot \nabla \mathbf{F} = -\Delta \mathbf{F}$ due to Gauss theorem $\nabla \cdot \mathbf{F} = 0$, $\mathbf{F} = \mathbf{E}, \mathbf{H}$ in the homogeneous, source free medium. The roots of the above equation are

$$\lambda_{j;1,2} = 1 + \frac{\Delta t^2 c^2 \Delta}{2} \pm \frac{i}{2} \sqrt{-\Delta t^2 c^2 \Delta (4 + \Delta t^2 c^2 \Delta)}, \quad (33)$$

which requires the following condition to be satisfied

$$0 \leq -\Delta t^2 c^2 \Delta \leq 4, \quad (34)$$

in order to ensure $|\lambda_{j;1,2}| \leq 1$. Finally, we arrive at the same stability condition as equation 41 of Mittet (2010),

$$\Delta t c_{\max} \sqrt{(D_x^{\max})^2 + (D_y^{\max})^2 + (D_z^{\max})^2} \leq 2, \quad (35)$$

where D_x^{\max} , D_y^{\max} and D_z^{\max} are the maximum value of the the discretized first derivatives along x , y and z directions. Let us emphasize this condition applies to both uniform and nonuniform grid. The difference lies in the spatial derivative operator.

To proceed with the stability analysis, we represent the fields on the grid via time harmonic plane waves

$$\mathbf{E}', \mathbf{H}' \propto e^{-i(\omega t - k_x x - k_y y - k_z z)}, \quad (36)$$

where the amplitude has been omitted. Equation 13 becomes

$$\begin{cases} D_x^+ u(x_I) = (\alpha_L(x_I) e^{ik_x(x_{I+L}-x_I)} + \alpha_{L-1}(x_I) e^{ik_x(x_{I+L-1}-x_I)} + \dots + \alpha_{-L+1}(x_I) e^{ik_x(x_{I-L+1}-x_I)}) u(x_I) \\ D_x^- u(x_i) = (\alpha_L(x_i) e^{ik_x(x_{I+L-1}-x_i)} + \alpha_{L-1}(x_i) e^{ik_x(x_{I+L-1}-x_i)} + \dots + \alpha_{-L+1}(x_i) e^{ik_x(x_{I-L}-x_i)}) u(x_i) \end{cases}. \quad (37)$$

Hence, we end up with the maximum possible values for discrete first derivative operators

$$D_x^{\max} = \max \left(\sum_{l=-L+1}^L |\alpha_l(x_I)|, \sum_{l=-L+1}^L |\alpha_l(x_l)| \right) \quad (38)$$

and similar estimations for D_y^{\max} and D_z^{\max} . In case of a uniform grid, the above expressions becomes much simpler

$$\begin{cases} D_x^+ u(x_I) = (\alpha_L e^{ik_x(L-1/2)\Delta x} + \alpha_{L-1} e^{ik_x(L-3/2)\Delta x} + \dots + \alpha_{-L+1} e^{ik_x(-L+1/2)\Delta x}) u(x_I) \\ D_x^- u(x_i) = (\alpha_L e^{ik_x(L-1/2)\Delta x} + \alpha_{L-1} e^{ik_x(L-3/2)\Delta x} + \dots + \alpha_{-L+1} e^{ik_x(-L+1/2)\Delta x}) u(x_i) \end{cases},$$

where Δx stands for the uniform grid spacing in x direction, while the coefficients α_l (which can be computed by inverting a Vandermonde matrix system according to Appendix A5) are independent of the location x_i .

2.3 Grid stretching

Our finite-difference modelling is carried out on a rectilinear mesh, which can be generated from the tensor (outer) product of 1D non-equispaced meshes. We use the geometrical progression to generate the 1D nonuniform grid, following the work of Mulder (2006, Appendix C). This is also often referred to as power law grid stretching since the cell sizes stretch exponentially to guarantee a smooth extension of the grid.

Assume we have the total grid length L_x divided into n intervals ($n+1$ nodes) with a common ratio $r > 1$. Denote the smallest interval $\Delta x = x_1 - x_0$. Thus, the relation between L_x and Δx is

$$L_x = (x_1 - x_0) + (x_2 - x_1) + \dots + (x_n - x_{n-1}) = \Delta x(1 + r + \dots + r^{n-1}) = \Delta x \frac{r^n - 1}{r - 1}. \quad (39)$$

Given the total distance L_x , the smallest grid spacing Δx and the stretching factor r , we can compute an approximate value for the number of nodes $n = \left\lceil \frac{\ln(1 + \frac{L_x}{\Delta x}(r-1))}{\ln(r)} \right\rceil$ following Mulder (2006), where $\lceil \cdot \rceil$ takes the ceiling integer value. This strategy yields approximate solution as the value of L_x is not exactly preserved.

Due to the stability requirement and the resulting computational cost in the modelling, we are restricted to the smallest interval Δx and a given number of intervals n to discretize over a certain distance L_x . The question boils down to finding an optimal growth factor r . This problem is more complicated since equation 39 does not yield an explicit expression for the stretching factor r .

The relation in equation 39 is equivalent to

$$r = \underbrace{\left(\frac{L_x}{\Delta x} (r-1) + 1 \right)^{\frac{1}{n}}}_{g(r)}, \quad (40)$$

which inspires us to carry out a number of fixed point iterations until convergence:

$$r^{k+1} = g(r^k), \quad k = 0, 1, \dots \quad (41)$$

Assume r^* is the analytic solution such that $r^* = g(r^*)$. Thanks to Lagrange mean value theorem, the error estimation at $(k+1)$ -th iteration is linked with the error at k -th iteration via

$$|e^{k+1}| = |r^{k+1} - r^*| = |g(r^k) - g(r^*)| = |g'(\xi)(r^k - r^*)| = |g'(\xi)| |e^k|, \quad \xi \text{ between } r^k \text{ and } r^*. \quad (42)$$

It becomes evident that $e^k \rightarrow 0$ ($k \rightarrow \infty$) provided that $|g'(r)| < 1$. Starting from any initial guess $r^0 > 1$, the fixed point iteration scheme in equation 41 is guaranteed to converge since

$$|g'(r)| = \frac{L_x}{n\Delta x} \left(\frac{L_x}{\Delta x} (r-1) + 1 \right)^{1/n-1} = \frac{1}{n} (r^{-(n-1)} + r^{-(n-2)} + \dots + 1) < 1,$$

thanks to the relations in equations 39 and 40.

We note that within areas of constant r , the derivative-operator coefficients in equation 13 can be calculated from the $2L$ coefficients a_{-l} and a_l , such that

$$\begin{aligned} \alpha_{-l}(i) &= \frac{a_{-l}}{\Delta x r^i}, \\ \alpha_l(i) &= \frac{a_l}{\Delta x r^i}. \end{aligned} \quad (43)$$

Two solutions of the Vandermonde system are required in this case, one for operators valid on the reference grid and one for operators valid on the staggered grid.

2.4 Implementation

A number of techniques have been applied to achieve efficient and accurate 3D CSEM simulation. According to equation 6, the frequency-domain CSEM response is obtained by a time to frequency transform. The transform is using the complex frequency given in equation 7. This gives exponential damping of late arrivals as is discussed in more detail in Mittet (2015). The lowest frequency experiences the least damping in this transform and by that requires the longest simulation time. This allows us to bound the number of time steps to terminate the simulation when the lowest frequency component has converged. The convergence means that the frequency-domain field obtained by time integration has reached its steady state and later arrivals are damped to the degree that they do not contribute to the time integral.

The source and receiver locations may be arbitrarily distributed over the whole computational domain, not necessarily located at the nodes of the finite-difference grid. In case they do, interpolation is not required and we directly take the field from the grid; otherwise, we need interpolation operators extracted from the first row of the relevant $[\mathbf{V}^T]^{-1}$ matrices.

The CFL condition to achieve stable FDTD modelling dictates the timestep for a given spatial sampling. The air-wave travels at extremely high speed which does not allow us to use the local finite-difference stencil to simulate it. The air-water boundary condition is implemented in the Fourier-wavenumber domain following the method proposed by Oristaglio and Hohmann (1984) and Wang and Hohmann (1993) and using the extension to high-order schemes given in Mittet (2010).

To mimic wave propagation in unbounded domain, we use a truncated computation mesh surrounded by an artificial absorbing boundary using convolutional perfectly matched layer (PML) technique (Roden and Gedney, 2000), except the top air-water interface. To ease the implementation, we extend the domain with equal spacing based on the last finite-difference cell size in the interior domain. Our CPML implementation is very standard using all the parameter setups given in Komatitsch and Martin (2007).

3 Numerical examples

We now present three examples to demonstrate the merits of high-order finite differences using nonuniform staggered grids. The first two examples are using 1D resistivity models under shallow water and deep water scenarios. In the 1D case, the semi-analytic solution can be computed in the frequency-wavenumber domain as a reference to benchmark our results. The third example takes into account varying seafloor topography, in which a reference solution can be computed using `emg3d` software (Werthmüller et al., 2019).

In all of our modelling, we use x-directed electrical dipole source. The E_x component at three commonly used frequencies - 0.25 Hz, 0.75 Hz and 1.25 Hz, are modelled. In total 12 layers of CPML are sufficient to achieve nearly perfect absorbing effect. The computed electromagnetic fields are normalized by the source current. The convergence check has been conducted every 100 time steps to avoid modelling after the frequency-domain EM fields stop evolving. We examine the amplitude error by inspecting the ratio of the modelled field to the reference solution, $|E_x^{FD}|/|E_x^{ref}|$, which should be close to unity if the modelling is precise. The phase difference is computed by $\angle E_x^{FD} - \angle E_x^{ref}$ in degrees.

3.1 Moving to high-order schemes

The model shown in Figure 3 includes 5 layers: the top is the air, then a 325 m layer of sea water with a resistivity of 0.3 Ωm , followed by three layers of formation with increasing resistivity in the depth direction. The whole model extends down to 5 km depth below the sea surface. A horizontal electrical dipole source is deployed at 275 m water depth, its lateral position being in the middle of the model. The EM fields are recorded using 201 receiver positions at the seafloor. The offsets range from -10 km to +10 km (receiver separation equals 100 m).

We first compare the 3D CSEM response simulated by FDTD with the reference solution calculated using `empymod` program (Werthmüller, 2017). To limit the factors affecting the modelling accuracy, this experiment has been done using isotropic modeling and uniform grid spacing ($\Delta x = \Delta y = 150$ m, $\Delta z = 50$ m). Panels (a) and (b) in Figure 4 shows the amplitude and the phase of the modelled EM fields by FDTD of 2nd order, which is highly consistent to the reference solution. At the offset beyond 1 km, the agreement between finite-difference and the analytical solution is good. The kink in the transition of the near-to-far offset in the amplitude response for all frequencies is a manifestation of the strong air-wave effect. In the very near field, where the receivers are located just below the transmitter, the phase exhibits a 180° jump due to the change in the direction of the electric field immediately below the electric dipole source. Due to the extension of finite-difference stencil, this phase rollover becomes smeared compared to the reference solution. For the same reason, finite difference

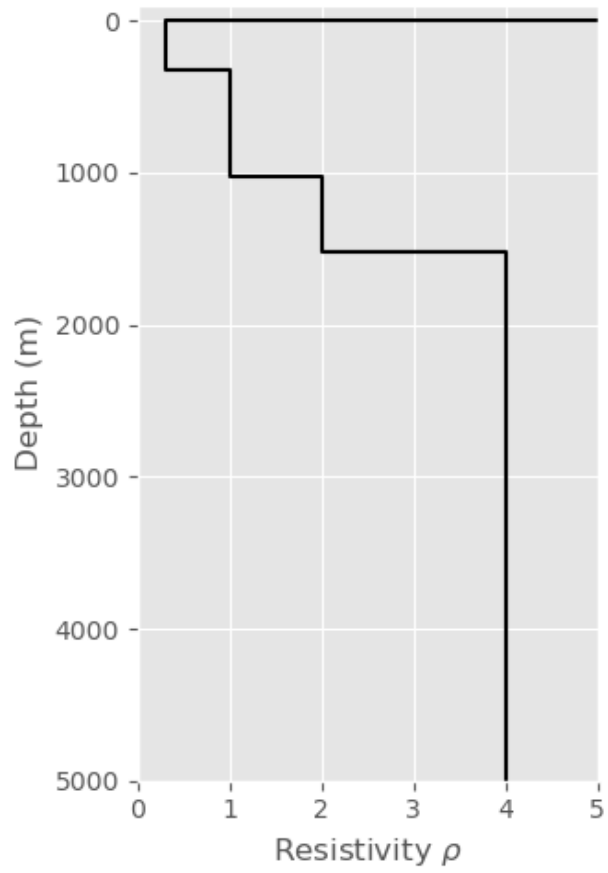


Figure 3: The resistivity model with air ($\rho = 10^{12} \Omega\text{m}$), shallow column (325 m) of $0.3 \Omega\text{m}$ and 3 sediment layers ($\rho = 1 \Omega\text{m}$ in $[325, 1025]$ m; $\rho = 2 \Omega\text{m}$ in $[1025, 1525]$ m; $\rho = 4 \Omega\text{m}$ downwards).

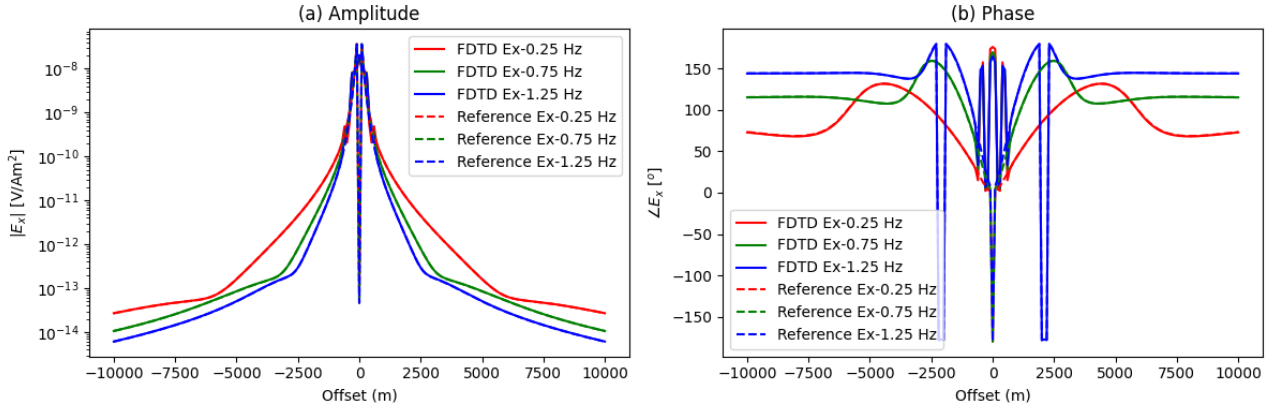


Figure 4: Comparison between 2nd order FDTD (solid line) and reference solution (dash line) for 3D CSEM simulation in the shallow water scenario. The horizontal coordinates are offsets, while the vertical coordinates are (a) Amplitude; (b) Phase.

Table 1: Comparison of computing time using FDTD of orders 2, 4 and 6.

FDTD	Order-2	Order-4	Order-6
Time (s)	422.3	715.5	1090.9

method introduces significant errors in the near field in amplitude (which becomes more evident for high-order schemes). Fortunately it is not an issue for practical 3D CSEM applications since the CSEM inversion to deduce the subsurface resistivity is mainly driven by far offset refractions. We thus focus on the analysis of the amplitude and phase error beyond 1 km offset in the following.

The modelling results by FDTD of higher orders are not displayed in Figure 4, since they are visually very similar to the reference solution. Instead, the amplitude and phase error are computed using 1D reference solution to examine the accuracy of our methods. In Figure 5a, c and e, we clearly see that the 2nd order FDTD gives the largest amplitude error for all frequencies; moving from 2nd order to 4th order significantly reduces the amplitude error, while moving to 6th order behaves even better, although the accuracy improvement becomes less. The phase errors exhibit a similar behavior.

In principle, the computational cost of the 4th order and the 6th order finite differences will be double and triple of that for the 2nd order scheme. Table 1 lists the CPU time for these modelling exercises, running on a laptop possessing Intel(R) Core(TM) i7-4710HQ CPU @ 2.50GHz. It shows the increase of the computing cost by increasing the order of FDTD scheme. The computing time of the 4th order scheme is less than two times the computing time of the 2nd order scheme. Further increase of the FDTD order results in significant increase of CPU time. Since moving to the 6th order scheme demands more computation while the accuracy improvement is marginal, we stay with the 4th order scheme from now on, as it gives the best compromise between increased accuracy and computational load.

3.2 The impact of nonuniform grid

The above example demonstrates the importance of higher order scheme to achieve accurate CSEM modeling in the presence of strong air-wave. We now examine the impact of grid non uniformity in achieving computational efficiency for high-order staggered grid FDTD. To get rid of the impact of air-wave, we consider a resistivity model in deep water scenario. As shown in Figure 6a, the model has 1020 m water column of $0.3 \Omega\text{m}$, followed by formation of $1\Omega\text{m}$ down to 1900 m, and 120 m thickness of resistor of $50 \Omega\text{m}$. The background resistivity below the resistor is $2.5 \Omega\text{m}$. To mimic a vertical transverse isotropic (VTI) Earth, all layers below the seabed are assigned with an anisotropy ratio (defined as $\lambda = \rho_v/\rho_h$ in this paper) $\lambda = 1.5$. The source is placed in the middle of the model, 40 m above the receivers sitting on the seabed. The resistivity in the water column and the formation above 1200 m was discretized with constant grid spacing: $\Delta x = \Delta y = 150 \text{ m}$, $\Delta z = 40 \text{ m}$. From 1200 m down to the bottom of the resistivity model, the grid has been stretched with different growing factors.

Figure 7a displays the stretching factor r of the nonuniform grid for different number of grid points n_z . Note that the cell size grows very fast with the factor r . For example, with $r = 1.05$ after 40 cells we obtain $r^{40} > 7$ times the size of the first cell. Let us now increase r (hence decrease n_z correspondingly) and analyze how it changes the total modelling time for the resistivity model of the same physical length in z direction. Figure 7b

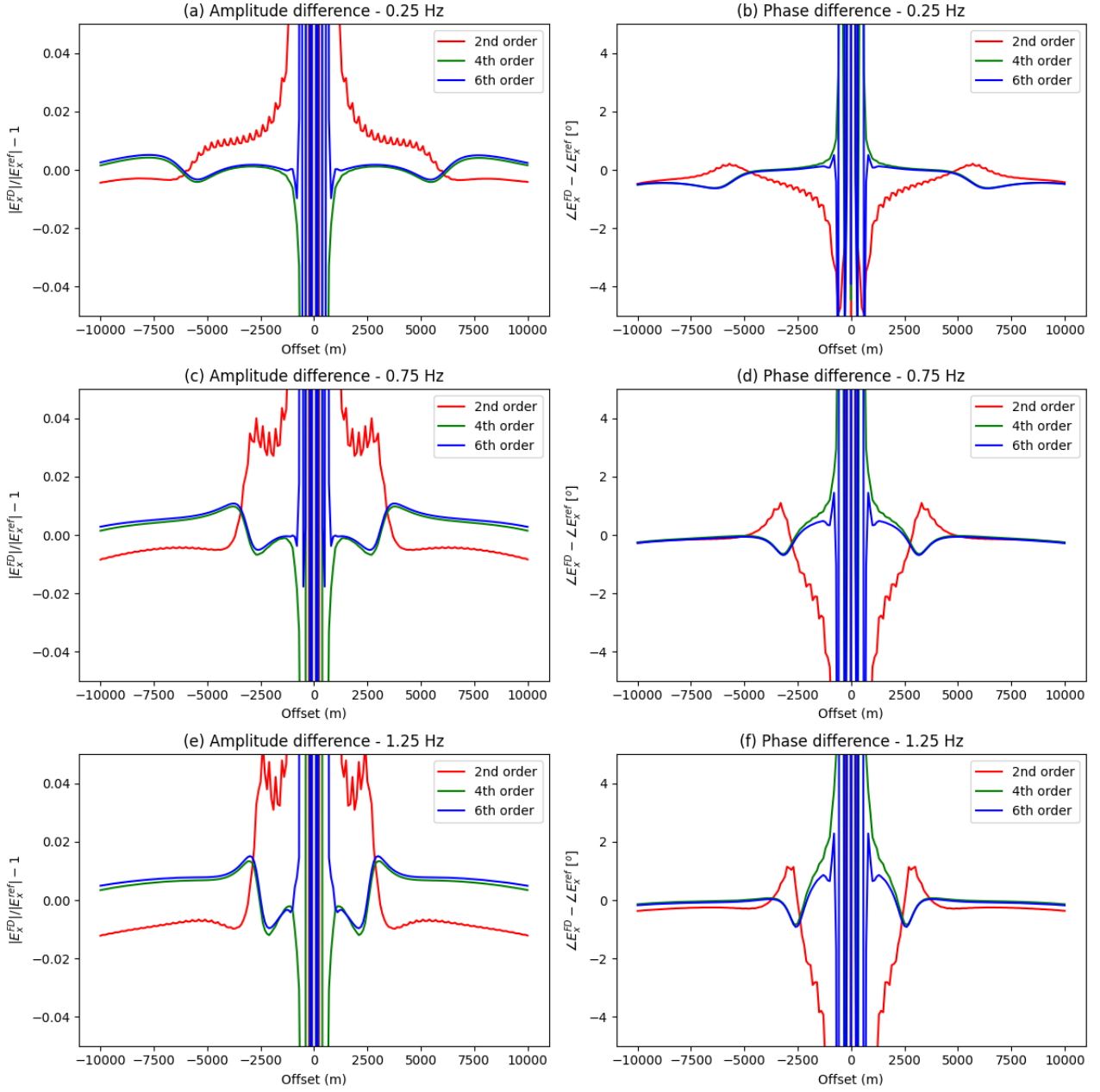


Figure 5: The amplitude and phase error of FDTD compared with 1D reference solution for 0.25 Hz (a,b), 0.75 Hz (c,d) and 1.25 Hz (e,f).

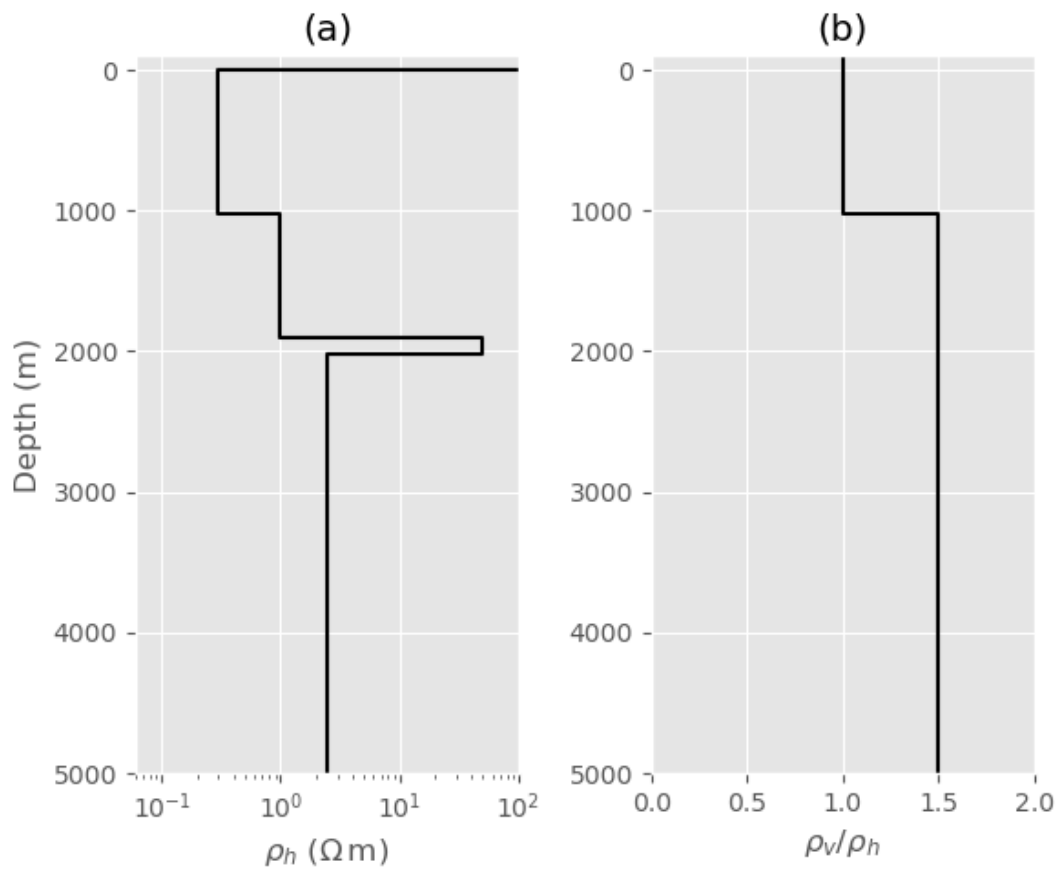


Figure 6: (a) The resistivity model in deep water: the 1020 m water column of 0.3 Ωm followed by formation of 1 Ωm down to 1900 m, and 120 m thickness of resistor of 50 Ωm , while the background resistivity below the resistor is 2.5 Ωm ; (b) VTI anisotropy below seabed is 1.5.

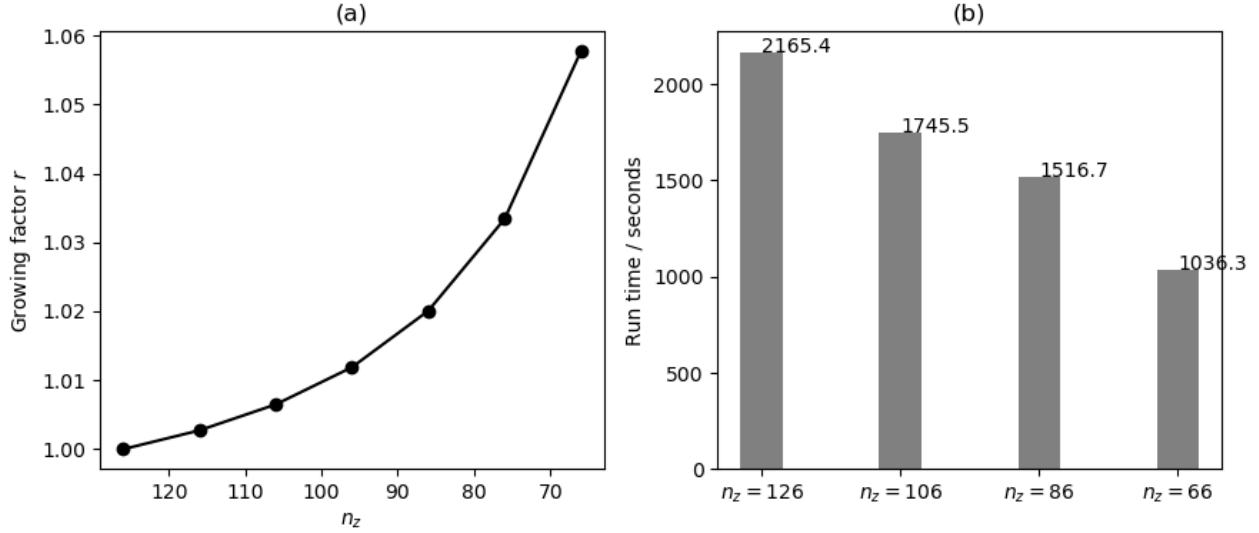


Figure 7: (a) The exponentially growing factor with the decreasing number of grid points n_z ; (b) With the decreasing number of grid points n_z , the modelling time decreases dramatically.

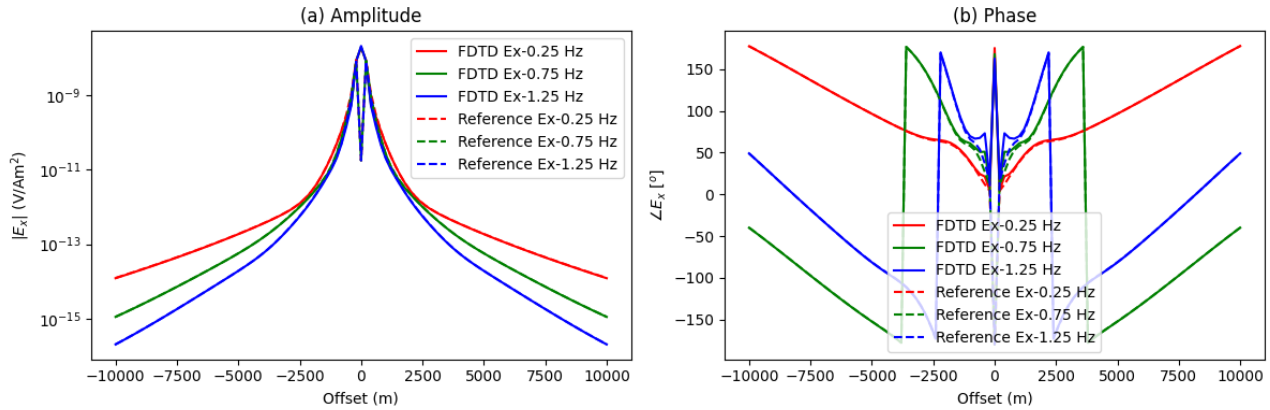


Figure 8: Comparison of (a) amplitude and (b) phase between 4th order FDTD (solid line) and reference solution (dash line) for 3D CSEM simulation in the deep water scenario.

displays a significant decrease of the modelling time associated with the reduction of the number of grid points n_z . We indeed see that modelling using $n_z = 66$ takes almost half of the simulation time compared to modelling using $n_z = 126$.

Figure 8 overlays the FDTD modelled EM fields with the reference solution. We see a very good agreement between the two in terms of both the amplitude and phase. To gain an idea of the modelling accuracy reduction when using less computing effort with nonuniform grid, we plotted the amplitude and phase errors in Figure 9 corresponding to three different frequencies. These figures clearly show that both the amplitude error and the phase error increase with the increase of the frequencies. It is also interesting to note that stretching the grid does not necessarily increase the amplitude error, but does increase the phase discrepancy. This highlights the importance of combination in examining both amplitude and phase.

3.3 3D modelling with seafloor bathymetry

The above 1D example highlights the importance of nonuniform grid in combination with high-order schemes to achieve efficient numerical modelling with sufficient accuracy. Here we consider a more realistic 3D resistivity model with bathymetry variations in horizontal directions, as shown in Figure 10a.

The model has seawater of $0.3 \Omega\text{m}$, followed by 2 formation layers of resistivity - $1 \Omega\text{m}$ and $2 \Omega\text{m}$. A resistor of $50 \Omega\text{m}$ was buried in the last formation layer to mimic a hydrocarbon bearing formation located between

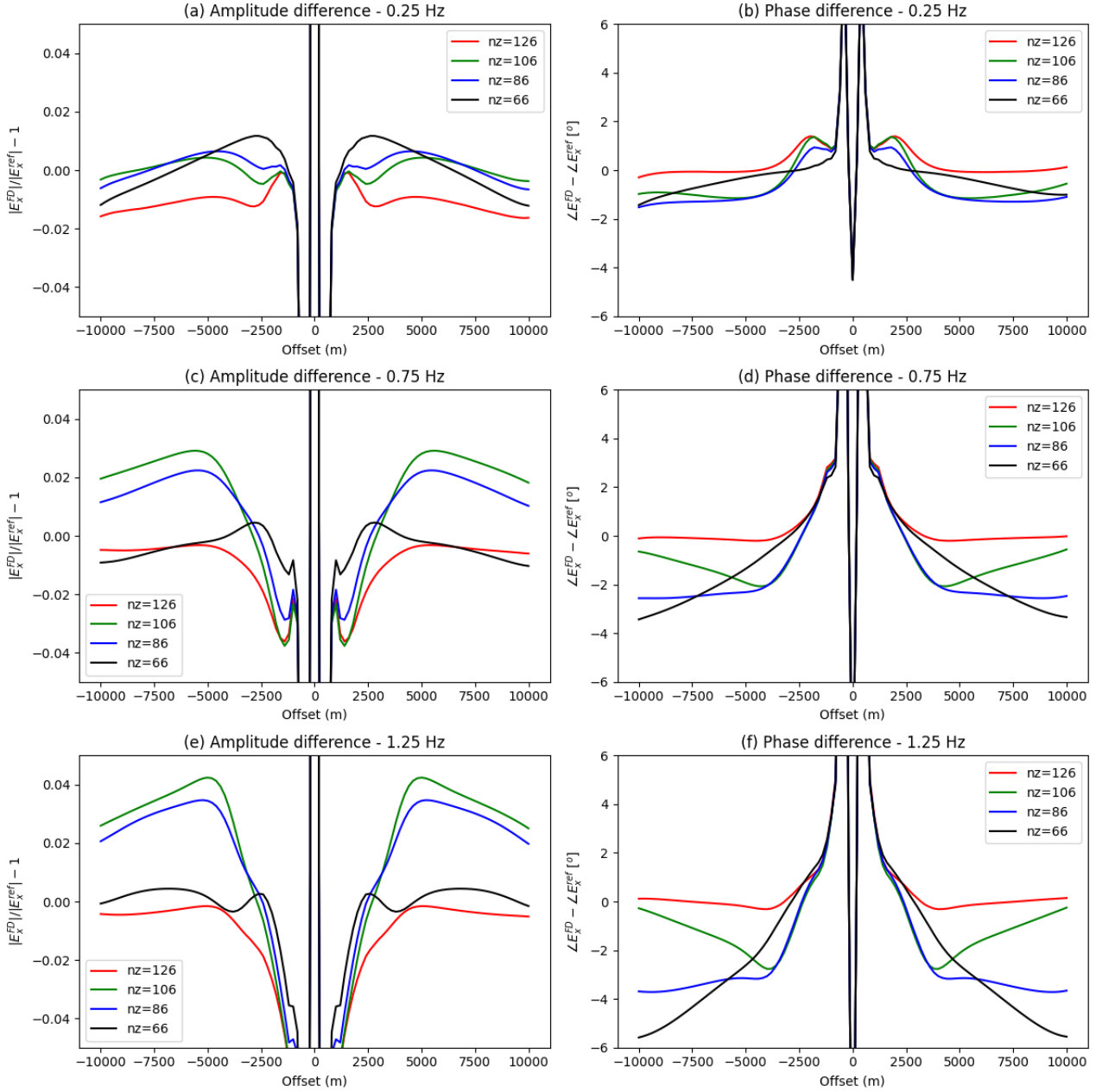


Figure 9: The amplitude and phase error of FDTD compared with 1D reference solution for 0.25 Hz (a,b), 0.75 Hz (c,d) and 1.25 Hz (e,f) in deep water.

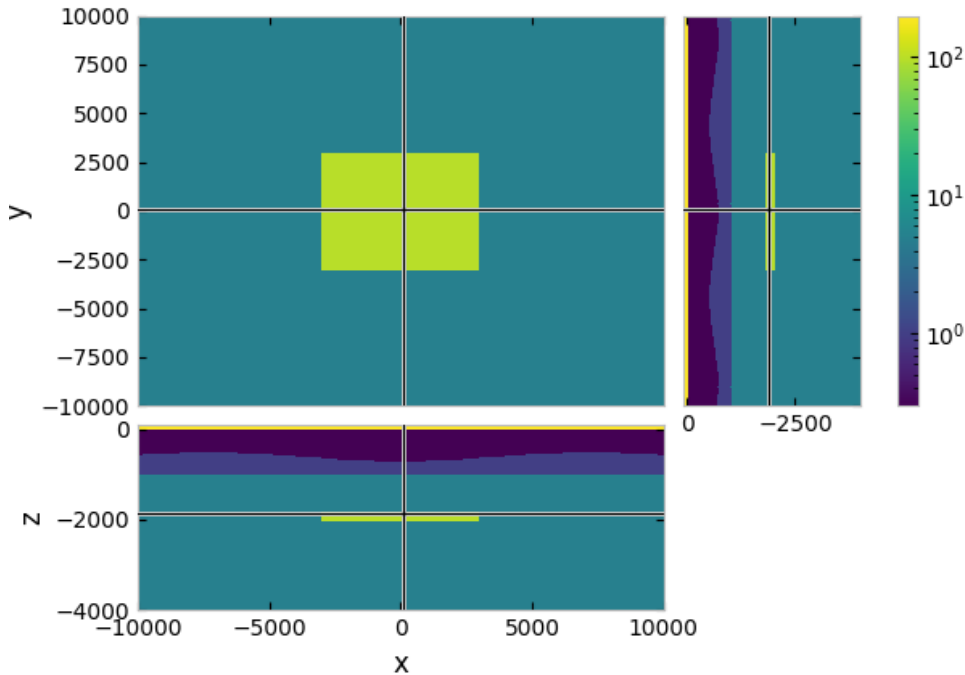


Figure 10: The 3D resistivity model with seafloor bathymetry, followed by 2 formation layers of resistivity values $1 \Omega\text{m}$ and $2 \Omega\text{m}$. The last sediment layer includes a strong resistor of $100 \Omega\text{m}$ mimicking a hydrocarbon bearing formation located within the depth range $[1800, 2000]$ m and the offset range $[-3000, 3000]$ m in both x and y directions. The source was placed at the center of the model while 101 receivers with 200 m spacing are deployed along x direction.

1800 m and 2000 m in depth, with the offset expanding from -3000 m to 3000 m in both x and y directions.

In order to validate the modelling accuracy of the proposed method, we simulated a reference solution by finite integration method in frequency domain using `emg3d` (Werthmüller et al., 2019). The finite-integration modelling extends the model tens of kilometers in each direction, to mimic that the EM fields propagate to very far distance while avoiding possible edge/boundary effects. In our finite-difference modelling, the PML boundary condition attenuates the artificial reflections in the computational domain within ten grid nodes to achieve the same behavior. A dipole source was placed at 650 m depth in the middle of the model, while 101 receivers are sitting on the curved seabed.

Figure 11 displays the comparison of the 3D CSEM modelling between our method and the result from `emg3d`. From the Figures 11a and 11b, both the amplitude and the phase from our method match very well with the reference solution. The maximum amplitude discrepancy for all frequencies in Figure 11c is bounded within 5% at most of the relevant offset. The maximum mismatch in phase is less than 1 degree for 0.25 Hz and 2 degrees for 0.75 Hz and 1.25 Hz for the EM field above the noise level ($1e-15 \text{ V/m}^2$), as can be seen in Figure 11d. These demonstrate the good accuracy achieved by our method.

4 Discussion

A natural idea to achieve higher modelling accuracy is to use denser sampling. However, increasing the number of grid points in each dimension will lead to exponentially growing computational overhead, i.e., double the sampling in x, y and z coordinates results in eight times more nodes in the simulation. Over the same domain the node separations are reduced with a factor of two. By that, the stability criterion dictates a reduction in the time step by a factor of two. The net result is an increase of computational cost with a factor of sixteen. This is significantly more costly than considering high-order FDTD. For a fixed error requirement, high-order FDTD has been demonstrated to be much more efficient than a lower-order scheme with dense sampling (Yefet and Petropoulos, 2001). Assuming a linear scaling dependency between computing time and the number of grid points, doubling the length of the finite-difference operator in x, y and z directions will simply double the

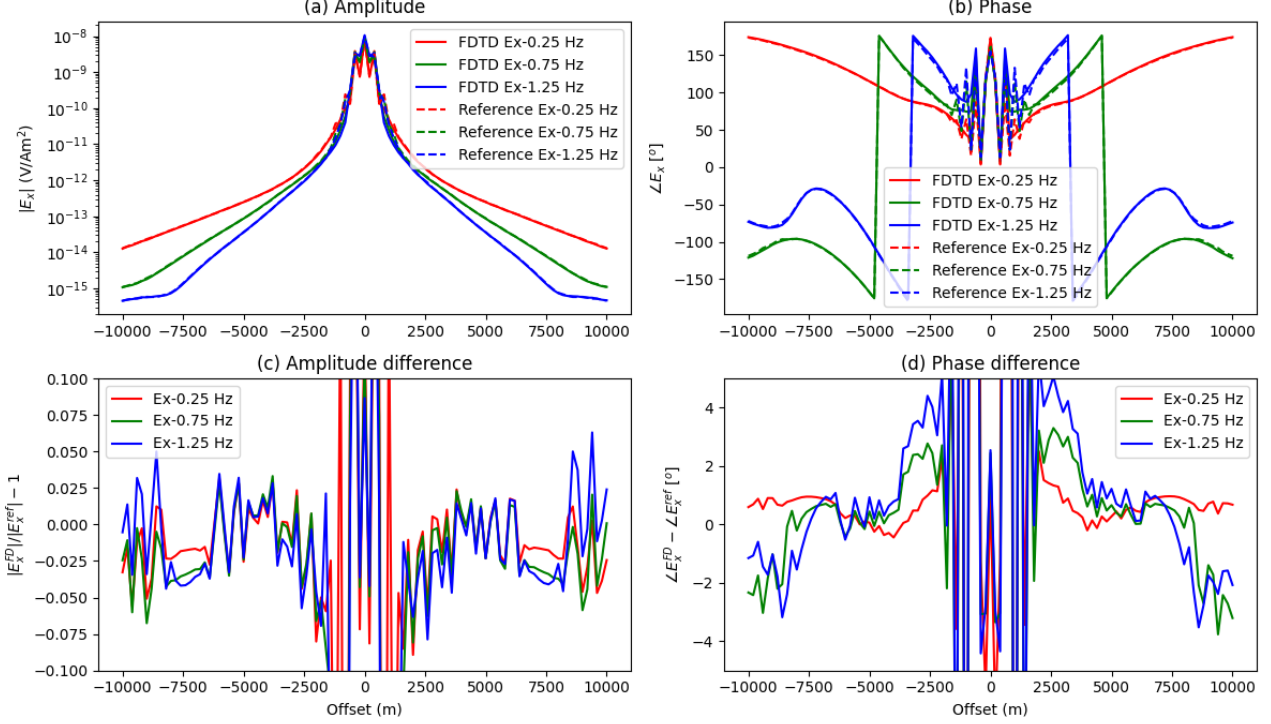


Figure 11: Comparison of the modelling results between the proposed method and the reference solution.

computational cost.

Stretching along z -direction seems always to be beneficial in terms of computational efficiency. It reduces the computational cost in two ways: first, it leads to increased grid spacing, hence less grid points and larger node spacing to discretize the resistivity model for simulation on the same physical size. Meanwhile, larger grid spacing permits to use a larger temporal step in terms of stability condition. This decreases the number of time steps needed to reach the steady state of the frequency-domain EM fields.

It is natural to stretch the nonuniform grid in all three spatial directions, with the motivation to decrease the computational cost further. In case there is no a priori knowledge about the subsurface, a possible practice is to start stretching from a given offset from the source location in the horizontal directions. This approach is not followed up here due to the fact that grid stretching complicates the calculation of the air-wave for time-domain codes. Grid stretching is applicable also for frequency-domain finite-difference codes. The airwave implementation is very different for frequency-domain codes, where the air layer is part of the simulation domain. Frequency-domain codes lend themselves easily to both vertical and horizontal grid stretching.

More research must be invested with respect to increasing the simulation efficiency of time-domain finite-difference schemes focusing on airwave implementation combined with horizontally nonuniform grids. The root of the problem is that the most common airwave implementations require fast Fourier transform (FFT) on regular grids. The fields are transformed to the wavenumber domain, propagated into the air layer in this domain and then transformed back to the space domain. A straight forward approach is to use interpolation between the uniform grid and the nonuniform one, as illustrated in Figure 12. The grid stretching in x - and y - directions certainly complicates the implementation while introducing additional computational cost, which is opposite to what we want to achieve. We have tested horizontal stretching for the previous 1D model using the stretching factor 1.05 in both x - and y - directions. The resulting amplitude and phase error in Figure 13 shows that the numerical accuracy is highly degraded (maximum amplitude error for 0.25 Hz is around 4%) compared with the result for a horizontally uniform grid (maximum amplitude error is less than 1.5% for all calculated frequencies). The running time is in fact longer than for the horizontally uniform grid which has a higher number of nodes. Due to the nonuniform grid staggering, several nodes on the uniform grid may reside in the same interval between two neighboring nodes on the nonuniform grid. The error panel displays an unsymmetrical pattern in Figure 13. Interpolating the fields from the uniform grid back to nonuniform grid can thus produce less accurate solutions. No stretching is therefore recommended along x - and y - for efficiency and accuracy considerations until a more accurate solution to this problem is developed.

It is noteworthy that fictitious wave domain is simply a mathematical tool to compute correct frequency

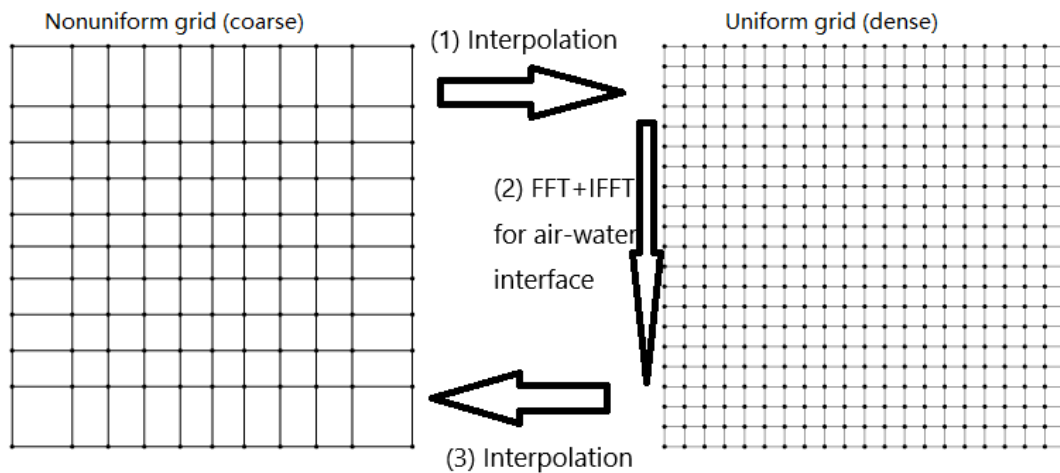


Figure 12: Horizontal grid stretching requires interpolating between the coarse nonuniform grid and a dense uniform grid, due to the equidistance requirement of FFT in airwave manipulation.

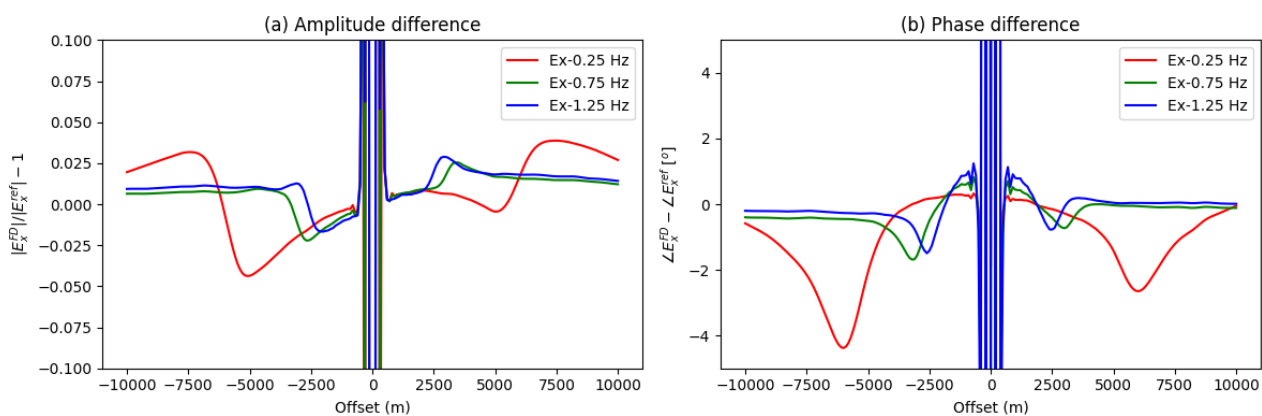


Figure 13: The amplitude and phase error after horizontal stretching of the 1D model with a stretching factor 1.05 along both x - and y - directions.

domain EM response efficiently by time stepping. The fictitious time is different from real time. To compute the true EM time series correctly, one needs to simulate a large number frequencies of the CSEM fields and then perform inverse Fourier transform, as has been done in Mittet (2010) and Rochlitz et al. (2021).

5 Conclusion

We have presented a 3D CSEM modelling method using high-order FDTD on a nonuniform grid. The key problem addressed in this work is the low accuracy and inconsistency issue in standard 2nd order staggered FDTD scheme on nonuniform grid. The strategy we propose is to adapt the interpolation weights depending on the nodal distance. These finite difference coefficients can be computed by inverting a Vandermonde matrix in an accurate and efficient manner. This makes our approach different from the commonly used EM modelling approaches. A new yet more generic stability condition has been established in order to achieve stable FDTD modelling. In designing the nonuniform grid based on geometrical progression, we develop a fixed point iteration to compute the optimal growing factor which allows good match of the modelling domain in case of grid stretching. The numerical examples demonstrate that there is a significant improvement in accuracy by using a high-order FDTD scheme, while combining it with a nonuniform grid reduces the computational cost without a significant sacrifice of accuracy. We conclude that high-order finite differences on nonuniform grid is a viable tool for full scale 3D CSEM modelling applications. Since the key idea is to use high order finite-difference coefficients adaptive to the node spacing, the method is expected to be applicable also for finite-difference frequency-domain schemes.

Acknowledgments

Pengliang Yang was supported by Chinese Fundamental Research Funds for the Central Universities (AUGA5710010121) and National Natural Science Foundation of China (42274156). Pengliang Yang thanks Dieter Werthermullter for the assistance to produce the reference solution using `empymod` and `emg3d` to validate the accuracy of the proposed method. The source code of this work can be found in the github repository: <https://github.com/yangpl/libEMM>.

Computing uniform staggered-grid finite difference coefficients via Vandermonde matrix inversion

The method to invert Vandermonde matrices gives us a generic approach to compute finite-difference coefficients with arbitrary grid spacing. A special case is the regular grid spacing. In what follows, we show how the standard staggered grid finite difference coefficients can be accurately computed also within the same framework.

The Taylor series expansion of a function $f(x)$ can be written as

$$\begin{cases} f(x+h) = f(x) + \frac{\partial f(x)}{\partial x} h + \frac{1}{2!} \frac{\partial^2 f(x)}{\partial x^2} h^2 + \frac{1}{3!} \frac{\partial^3 f(x)}{\partial x^3} h^3 + \dots \\ f(x-h) = f(x) - \frac{\partial f(x)}{\partial x} h + \frac{1}{2!} \frac{\partial^2 f(x)}{\partial x^2} h^2 - \frac{1}{3!} \frac{\partial^3 f(x)}{\partial x^3} h^3 + \dots \end{cases} \quad (44)$$

It leads to

$$\begin{cases} \frac{f(x+h)+f(x-h)}{2} = f(x) + \frac{1}{2!} \frac{\partial^2 f(x)}{\partial x^2} h^2 + \frac{1}{4!} \frac{\partial^4 f(x)}{\partial x^4} h^4 + \dots \\ \frac{f(x+h)-f(x-h)}{2} = \frac{\partial f(x)}{\partial x} h + \frac{1}{3!} \frac{\partial^3 f(x)}{\partial x^3} h^3 + \frac{1}{5!} \frac{\partial^5 f(x)}{\partial x^5} h^5 + \dots \end{cases} \quad (45)$$

Let $h = \Delta x/2$. This implies the 2nd order accuracy of centered finite difference scheme using only two staggered nodes

$$\begin{cases} \frac{\partial f(x)}{\partial x} = \frac{f(x+\Delta x/2)-f(x-\Delta x/2)}{\Delta x} + O(\Delta x^2) \\ f(x) = \frac{f(x+\Delta x/2)+f(x-\Delta x/2)}{2} + O(\Delta x^2) \end{cases} \quad (46)$$

To approximate the 1st order derivatives as accurate as possible, we express it using more consecutive nodes. Due to regular grid staggering, the coefficients lying on symmetric positions should have the same coefficients. This means the first-order derivative reads in the following form

$$\begin{aligned} \frac{\partial f}{\partial x} = & b_1 \frac{f(x+\Delta x/2) - f(x-\Delta x/2)}{\Delta x} + \\ & b_2 \frac{f(x+3\Delta x/2) - f(x-3\Delta x/2)}{3\Delta x} + \\ & b_3 \frac{f(x+5\Delta x/2) - f(x-5\Delta x/2)}{5\Delta x} + \dots \end{aligned} \quad (47)$$

Substituting the $f(x+h)$ and $f(x-h)$ with equation 44 for $h = \Delta x/2, 3\Delta x/2, \dots$ results in

$$\begin{aligned}
\frac{\partial f}{\partial x} &= b_1 \cdot 2 \left(\frac{\Delta x}{2} \frac{\partial f}{\partial x} + \frac{1}{3!} \left(\frac{\Delta x}{2} \right)^3 \frac{\partial^3 f}{\partial x^3} + \dots \right) / \Delta x \\
&+ b_2 \cdot 2 \left(\frac{3\Delta x}{2} \frac{\partial f}{\partial x} + \frac{1}{3!} \left(\frac{3\Delta x}{2} \right)^3 \frac{\partial^3 f}{\partial x^3} + \dots \right) / 3\Delta x \\
&+ b_3 \cdot 2 \left(\frac{5\Delta x}{2} \frac{\partial f}{\partial x} + \frac{1}{3!} \left(\frac{5\Delta x}{2} \right)^3 \frac{\partial^3 f}{\partial x^3} + \dots \right) / 5\Delta x + \dots \\
&= (b_1 + b_2 + b_3 + b_4 + \dots) \frac{\partial f}{\partial x} \\
&+ \frac{\Delta x^2}{3! \cdot 2^2} (b_1 + 3^2 b_2 + 5^2 b_3 + 7^2 b_4 + \dots) \frac{\partial^3 f}{\partial x^3} \\
&+ \frac{\Delta x^4}{5! \cdot 2^4} (b_1 + 3^4 b_2 + 5^4 b_3 + 7^4 b_4 + \dots) \frac{\partial^5 f}{\partial x^5} + \dots
\end{aligned} \tag{48}$$

Thus, taking first L terms (corresponding to using $2L$ nodes) requires

$$\begin{cases} b_1 + b_2 + b_3 + \dots + b_L & = 1 \\ b_1 + 3^2 b_2 + 5^2 b_3 + \dots + (2L-1)^2 b_L & = 0 \\ b_1 + 3^4 b_2 + 5^4 b_3 + \dots + (2L-1)^4 b_L & = 0, \\ \dots & \\ b_1 + 3^{2L-2} b_2 + 5^{2L-2} b_3 + \dots + (2L-1)^{2L-2} b_L & = 0 \end{cases} \tag{49}$$

which again builds up a Vandermonde-like system

$$\underbrace{\begin{bmatrix} 1 & 1 & \dots & 1 \\ x_1 & x_2 & \dots & x_L \\ \vdots & & \ddots & \vdots \\ x_1^{L-1} & x_2^{L-1} & \dots & x_L^{L-1} \end{bmatrix}}_{\mathbf{v}} \underbrace{\begin{bmatrix} b_1 \\ b_2 \\ \vdots \\ b_L \end{bmatrix}}_{\mathbf{b}} = \underbrace{\begin{bmatrix} 1 \\ 0 \\ \vdots \\ 0 \end{bmatrix}}_{\mathbf{z}}, \tag{50}$$

in which $x_i = (2i-1)^2$, $i = 1, \dots, L$. The finite difference weights can then be easily computed using Golub (1996, Algorithm 4.6.2), see an Octave/Matlab script for computing them in Yang (2014, section 2.5). These numerically computed weights may be cross-validated with the generic method by Fornberg (1988, Table 2). With regular grid spacing Δx , the weights b_i are dimensionless and can be connected to the coefficients α_i in equation 13 involving a scaling factor Δx .

References

- Björck, A., and V. Pereyra, 1970, Solution of Vandermonde systems of equations: *Mathematics of computation*, **24**, 893–903.
- da Silva, N. V., J. V. Morgan, L. MacGregor, and M. Warner, 2012, A finite element multifrontal method for 3D CSEM modeling in the frequency domain: *Geophysics*, **77**, E101–E115.
- de Hoop, A. T., 1996, A general correspondence principle for time-domain electromagnetic wave and diffusion fields: *Geophysical Journal International*, **127**, 757–761.
- Demmel, J., and P. Koev, 2005, The accurate and efficient solution of a totally positive generalized vandermonde linear system: *SIAM Journal on Matrix Analysis and Applications*, **27**, 142–152.
- Fornberg, B., 1988, Generation of finite difference formulas on arbitrarily spaced grids: *Mathematics of Computation*, **51**, 699–706.
- Golub, G. H., 1996, *Matrix computation*, third edition: Johns Hopkins Studies in Mathematical Sciences.
- Key, K., 2016, MARE2DEM: a 2-D inversion code for controlled-source electromagnetic and magnetotelluric data: *Geophysical Journal International*, **207**, 571–588.
- Komatitsch, D., and R. Martin, 2007, An unsplit convolutional perfectly matched layer improved at grazing incidence for the seismic wave equation: *Geophysics*, **72**, SM155–SM167.
- Lee, K. H., G. Liu, and H. Morrison, 1989, A new approach to modeling the electromagnetic response of conductive media: *Geophysics*, **54**, 1180–1192.

- Li, Y., and K. Key, 2007, 2D marine controlled-source electromagnetic modeling: Part 1—an adaptive finite-element algorithm: *Geophysics*, **72**, WA51–WA62.
- Maaø, F., 2007, Fast finite-difference time-domain modeling for marine subsurface electromagnetic problems: *Geophysics*, **72**, A19–A23.
- Mittet, R., 2010, High-order finite-difference simulations of marine CSEM surveys using a correspondence principle for wave and diffusion fields: *Geophysics*, **75**, F33–F50.
- , 2015, Seismic wave propagation concepts applied to the interpretation of marine controlled-source electromagnetics: *Geophysics*, **80**, E63–E81.
- , 2017, On the internal interfaces in finite-difference schemes: *Geophysics*, **82**, T159–T182.
- Monk, P., and E. Süli, 1994, A convergence analysis of Yee’s scheme on nonuniform grids: *SIAM Journal on Numerical Analysis*, **31**, 393–412.
- Mulder, W., 2006, A multigrid solver for 3D electromagnetic diffusion: *Geophysical prospecting*, **54**, 633–649.
- Newman, G. A., and D. L. Alumbaugh, 1995, Frequency-domain modelling of airborne electromagnetic responses using staggered finite differences: *Geophysical Prospecting*, **43**, 1021–1042.
- Oristaglio, M. L., and G. W. Hohmann, 1984, Diffusion of electromagnetic fields into a two-dimensional earth: A finite-difference approach: *Geophysics*, **49**, 870–894.
- Puzryev, V., J. Koldan, J. de la Puente, G. Houzeaux, M. Vázquez, and J. M. Cela, 2013, A parallel finite-element method for three-dimensional controlled-source electromagnetic forward modelling: *Geophysical Journal International*, **193**, 678–693.
- Rochlitz, R., M. Seidel, and R.-U. Börner, 2021, Evaluation of three approaches for simulating 3-D time-domain electromagnetic data: *Geophysical Journal International*, **227**, 1980–1995.
- Rochlitz, R., N. Skibbe, and T. Günther, 2019, cistem: Customizable finite-element simulation of complex controlled-source electromagnetic data: *Geophysics*, **84**, F17–F33.
- Roden, J. A., and S. D. Gedney, 2000, Convolution PML (CPML): An efficient FDTD implementation of the CFS-PML for arbitrary media: *Microwave and optical technology letters*, **27**, 334–339.
- Smith, J. T., 1996a, Conservative modeling of 3-D electromagnetic fields, Part i: Properties and error analysis: *Geophysics*, **61**, 1308–1318.
- , 1996b, Conservative modeling of 3-D electromagnetic fields, Part II: Biconjugate gradient solution and an accelerator: *Geophysics*, **61**, 1319–1324.
- Streich, R., 2009, 3D finite-difference frequency-domain modeling of controlled-source electromagnetic data: Direct solution and optimization for high accuracy: *Geophysics*, **74**, F95–F105.
- Taflove, A., and S. C. Hagness, 2005, *Computational electrodynamics: The finite-difference time-domain method*, 3rd ed.: Artech House.
- Wang, T., and G. W. Hohmann, 1993, A finite-difference, time-domain solution for three-dimensional electromagnetic modeling: *Geophysics*, **58**, 797–809.
- Werthmüller, D., 2017, An open-source full 3D electromagnetic modeler for 1D VTI media in Python: *empymod*: *Geophysics*, **82**, WB9–WB19.
- Werthmüller, D., W. Mulder, and E. Slob, 2019, emg3d: A multigrid solver for 3d electromagnetic diffusion: *Journal of Open Source Software*, **4**, 1463.
- Yang, P., 2014, A numerical tour of wave propagation: Technical report, Xi’an Jiaotong University.
- Yee, K. S., 1966, Numerical solution of initial boundary value problems involving Maxwell’s equations in isotropic media: *IEEE Transactions on Antennas and Propagation*, **14**, 302–307.
- Yefet, A., and P. G. Petropoulos, 2001, A staggered fourth-order accurate explicit finite difference scheme for the time-domain maxwell’s equations: *Journal of Computational Physics*, **168**, 286–315.